

PolyFormer: learning efficient reformulations for scalable optimization under complex physical constraints

Yilin Wen^{1,2†}, Yi Guo^{3†}, Bo Zhao^{1*}, Wei Qi^{4*}, Zechun Hu^{2*},
Colin Jones⁵, Jian Sun³

¹School of Electrical and Electronic Engineering, North China Electric Power University, Changping District, Beijing, 102206, China.

²Department of Electrical Engineering, Tsinghua University, Haidian District, Beijing, 100084, China.

³School of Automation, Beijing Institute of Technology, Haidian District, Beijing, 100081, China.

⁴Department of Industrial Engineering, Tsinghua University, Haidian District, Beijing, 100084, China.

⁵Laboratory for Systems and Control, École Polytechnique Fédérale de Lausanne (EPFL), Station 9, Lausanne, 1015, Switzerland.

*Corresponding author(s). E-mail(s): zhaobozju@163.com;
qiwei@tsinghua.edu.cn; zechhu@tsinghua.edu.cn;

Contributing authors: wenyl@ncepu.edu.cn; yi.guo@bit.edu.cn;
colin.jones@epfl.ch; sunjian@bit.edu.cn;

†These authors contributed equally to this work.

Abstract

Real-world optimization problems are often constrained by complex physical laws that limit computational scalability. These constraints are inherently tied to complex regions, and thus learning models that incorporate physical and geometric knowledge, i.e., physics-informed machine learning (PIML), offer a promising pathway for efficient solution. Here, we introduce PolyFormer, which opens a new direction for PIML in prescriptive optimization tasks, where physical and geometric knowledge is not merely used to regularize learning models, but to simplify the problems themselves. PolyFormer captures geometric structures behind constraints and transforms them into efficient polytopic reformulations, thereby

decoupling problem complexity from solution difficulty and enabling off-the-shelf optimization solvers to efficiently produce feasible solutions with acceptable optimality loss. Through evaluations across three important problems (large-scale resource aggregation, network-constrained optimization, and optimization under uncertainty), PolyFormer achieves computational speedups up to 6,400-fold and memory reductions up to 99.87%, while maintaining solution quality competitive with or superior to state-of-the-art methods. These results demonstrate that PolyFormer provides an efficient and reliable solution for scalable constrained optimization, expanding the scope of PIML to prescriptive tasks in scientific discovery and engineering applications.

Keywords: Physics-informed machine learning, complex physical constraints, problem simplification, polytopic representation, scalable optimization

1 Introduction

Real-world optimization problems are governed by complex physical constraints that limit their scalability. Three prototypical sources of complexity are pervasive across domains: the large scale of entities involved, their interdependencies, and uncertainties. Numerous per-individual constraints arise in large-scale resource control or management [1–3]. Network interdependencies appear in communication [4], energy [5], and transportation [6] systems. Uncertainty-related constraints emerge in many scientific [7], engineering [8], or financial [9] decisions. These characteristics make optimization-based decision-making problems high-dimensional, nonlinear, and mixed-integer, substantially complicating the search for effective solutions. Such difficulties intensify as large-scale socio-technical systems continue to expand. For example, electric vehicles, whose planning and operation involve decision-making across power systems, transportation networks, and communication infrastructures, have increased by over eightyfold from 2014 to 2024 [10], dramatically increasing the dimensionality of decision spaces. As a result, scalable optimization for decision-making under complex constraints is becoming increasingly challenging. This challenge can lead to substantial social and economic impacts. For example, the 2025 blackout in Spain and Portugal was primarily caused by improper unit scheduling due to suboptimal power system decisions, affecting over 50 million people and resulting in direct economic losses exceeding 20 billion Euros [11]. Addressing the scalability gap in constrained optimization is therefore not merely a computational challenge, but a societal imperative.

Existing studies follow two main paradigms to address this challenge, but both face fundamental limitations. The first is analytical methods. These include decomposition and coordination that split large problems into smaller subproblems solved iteratively [12–14], convex relaxation approaches that approximate nonconvex constraints with tractable convex ones [15–17], and analytical surrogate models that simplify complex feasible regions [18–20]. While these methods provide theoretical guarantees, they often require problem-specific derivations, potentially suffer from unstable convergence, and may lack scalability across diverse constraint types. The second is based

on machine learning (ML). Some approaches directly predict optimization solutions [21, 22]. Others aim to accelerate solvers by learning branch-and-bound policies [23], generating warm starts [24], or improving heuristic search [25]. Prediction-based methods often lack feasibility guarantees and interpretability, and may also face training instability when applied to large-scale problems [26]. Solver-acceleration methods still require storing and operating on the full optimization model, and their worst-case solution times remain prohibitively long. These issues limit their use in real-time or memory-constrained settings.

In this context, physics-informed machine learning (PIML) has emerged as a natural integration of machine learning and the analytical modeling of physical laws or prior knowledge. By explicitly embedding physical principles into the learning framework, PIML improves data efficiency and ensures the physical consistency of the results [27]. This approach has led to advancements in various fields, including physics [28, 29], biology [30], chemistry [31], geosciences [32], and others. However, a closer examination of the literature reveals a significant gap: existing research has primarily focused on *predictive* tasks, where models are trained to satisfy differential equations or other physical constraints by minimizing residual errors. In contrast, *prescriptive* tasks involving high-dimensional or topologically complex constraints have not been fully explored within the PIML framework. In these tasks, current PIML architectures struggle to guarantee the reliability needed for valid solutions. Only a few attempts have been made to use physics-informed neural networks as surrogate models [33] or for direct solution prediction [34], but these approaches may conflict with optimization objectives and are difficult to generalize across different domains. This highlights a key question: while PIML has been widely used for predictive modeling, can it also serve prescriptive optimization tasks under complex physical constraints? Unlocking this capability requires a carefully designed adaptation of PIML, enabling it to produce feasible and near-optimal solutions.

Here, we present a new capability of PIML. Instead of using it to predict solutions or accelerate existing solvers, we introduce **PolyFormer**, a PIML framework that learns to *simplify the problem itself*. The key insight is that many complex constraints, despite their diverse forms, define a geometric shape that can be learned by PIML and approximated by a compact polytopic reformulation. By replacing the original constraints with their simplified polytopic representations, PolyFormer allows off-the-shelf optimization solvers to compute solutions more efficiently while maintaining feasibility and controlled optimality loss. PolyFormer is not a direct application of PIML to optimization, but a targeted design with three notable features: (1) it learns constraint geometry through an explicitly differentiable loss defined on approximating errors, which differs from existing fitting approaches; (2) it controls the trade-off between feasibility and optimality, allowing adaptation to different application requirements; and (3) it adapts to varying parameters through neural network parameterization, enabling fast re-estimation without retraining. These design features enable PolyFormer to address the three aforementioned prototypical challenges that limit scalability in optimization under complex physical constraints (see Fig. 1a).

We evaluate the performance of PolyFormer on three important problems that are representative of the three challenges in constrained optimization. First, to address

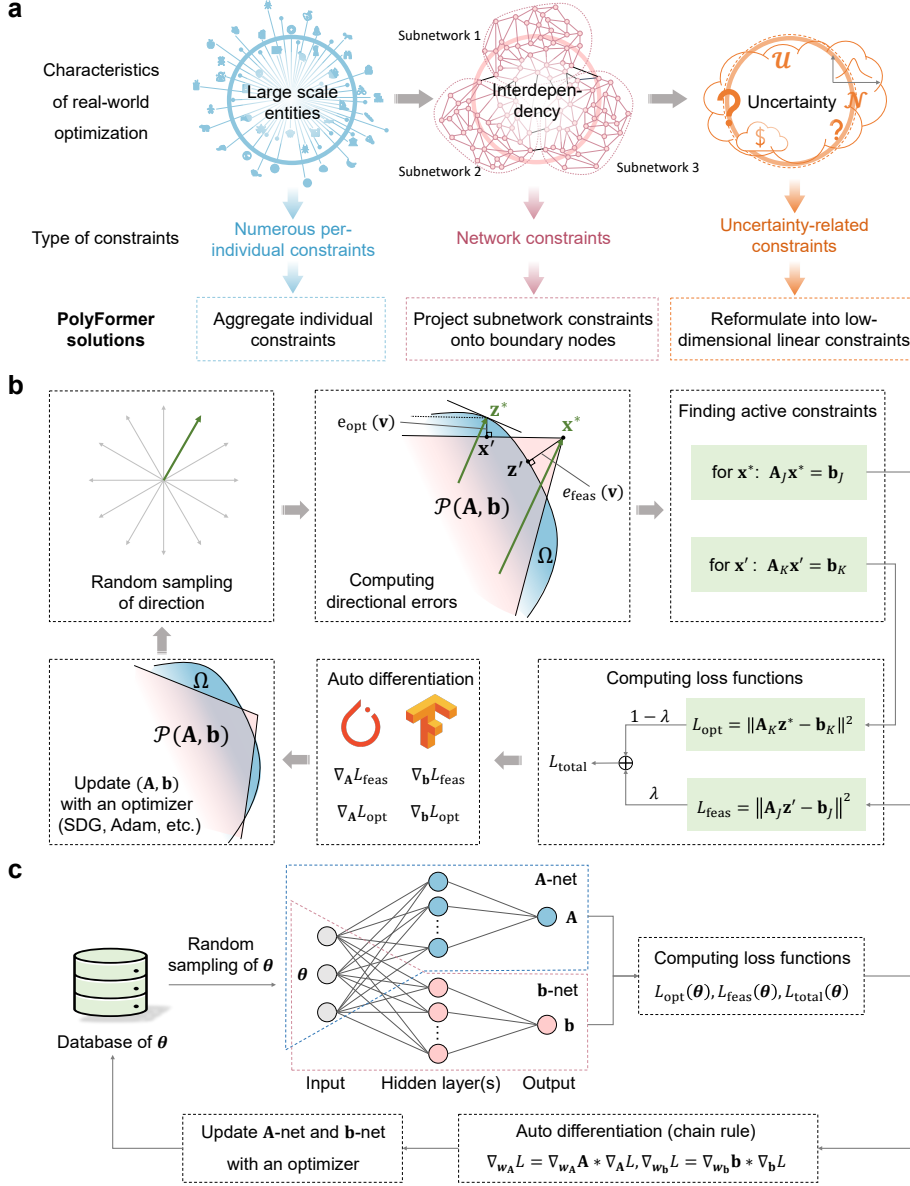


Fig. 1 Capability and training procedure of PolyFormer. **a**, PolyFormer solutions under three classes of complex physical constraints: large-scale per-individual constraints, network constraints, and uncertainty-related constraints. **b**, Training pipeline of PolyFormer. The procedure comprises six steps: (1) random sampling of a direction \mathbf{v} ; (2) computation of the directional feasibility and optimality errors, $e_{\text{feas}}(\mathbf{v})$ and $e_{\text{opt}}(\mathbf{v})$, together with the associated boundary points \mathbf{x}^* , \mathbf{z}' , \mathbf{z}^* and \mathbf{x}' (see “Error metrics” section in the Methods); (3) identification of active constraints in the current polytope at \mathbf{x}^* and \mathbf{x}' ; (4) evaluation of the loss based on the distance from \mathbf{z} to the hyperplanes defined by the active constraints; (5) gradient computation via automatic differentiation (see “Loss function and gradients” sections in the Methods); and (6) parameter updates of \mathbf{A} and \mathbf{b} using gradient-based optimization. **c**, Training of the parameterized PolyFormer additionally involves sampling a parameter θ and mapping it to $\mathbf{A}(\theta)$ and $\mathbf{b}(\theta)$ using two neural networks, denoted **A-net** and **b-net**, with trainable weights w_A and w_b , respectively.

the numerous per-individual constraints arising from the large-scale entities, PolyFormer learns to aggregate them to produce a compact set of constraints defined over aggregated variables. This reduces constraint counts by over 99% while maintaining accuracy superior to existing methods. PolyFormer also accommodates both continuous and discrete control inputs, extending beyond the capabilities of state-of-the-art approaches. Second, regarding the complex interdependencies among the entities, which are typically characterized by large-scale network constraints, PolyFormer projects subnetwork constraints onto boundary nodes, producing a polytopic feasible set defined solely over boundary node variables. Experimental results demonstrate up to a $6,400\times$ speedup and a 99.6% reduction in memory usage, while keeping the maximum feasibility and objective errors on the order of 10^{-10} and 10^{-4} , respectively. Third, for optimization under uncertainty-related constraints, whose standard formulations introduce substantial auxiliary variables, PolyFormer generates low-dimensional linear reformulations that reduce problem size from up to 1,044,497 constraints to 1,617, while identifying non-inferior, and in some cases strictly superior, solutions in terms of out-of-sample constraint satisfaction and objective improvement. Collectively, these results establish PolyFormer as a general framework for scalable optimization under complex physical constraints, underscoring the broad potential of PIML to enable more efficient and reliable solutions in prescriptive tasks.

2 Results

2.1 Overview of PolyFormer

Consider the original feasible region Ω of an optimization problem as a bounded, compact subset of the n -dimensional Euclidean space \mathbb{R}^n , generally formulated as

$$\Omega \triangleq \{\mathbf{x} | g_j(\mathbf{x}, \mathbf{y}) \leq 0, j = 1, 2, \dots, m\}, \quad (1)$$

Here, $\mathbf{x} \in \mathbb{R}^n$ denotes the variables of primary interest that the region Ω is defined for, while $\mathbf{y} \in \mathbb{R}^{n'}$ represents auxiliary variables that also influence Ω . When $n' = 0$, the problem reduces to a pure region fitting task in \mathbb{R}^n . In the more general case where $n' > 0$, the construction of Ω can be interpreted as a projection from the higher-dimensional space $\mathbb{R}^{n+n'}$ onto \mathbb{R}^n [35]. Both settings are handled in a unified manner within the PolyFormer framework. The integer m denotes the number of original constraints, and the inequalities $g_j(\mathbf{x}, \mathbf{y}) \leq 0$ encode the governing physical laws and operational limits that geometrically determine the shape of the region Ω .

PolyFormer aims to fit Ω using a polytope $\mathcal{P}(\mathbf{A}, \mathbf{b}) = \{\mathbf{x} | \mathbf{A}\mathbf{x} \leq \mathbf{b}\}$, where \mathbf{A} is an $M \times n$ matrix and \mathbf{b} is an M -dimensional vector. Here, M represents the number of hyperplanes that define the polytope \mathcal{P} , which is a pre-determined hyperparameter constrained by practical factors such as memory and computational time. If Ω is convex, then \mathcal{P} can approximate Ω to arbitrary precision provided that M is sufficiently large [36]. When Ω is non-convex or discontinuous, the current PolyFormer remains implementable, but the resulting polytope may approximate the convex hull of Ω rather than its exact geometry (see “Error metrics” and “Typical geometries”

sections in the Methods). Importantly, the convexity of Ω does not require each constraint function $g_j (\forall j = 1, 2, \dots, m)$ to be convex, nor does it require all variables to be continuous. In particular, assume that \mathbf{x} is continuous and $n' > 0$, even if the constraint functions g_j are non-convex and some components of \mathbf{y} are integer variables, the projected region Ω may still be convex since projection tends to preserve the convex envelope of a set while disregarding its internal concavities [37, Theorem 2.3].

The foundation of fitting is defining an appropriate error metric between the polytope $\mathcal{P}(\mathbf{A}, \mathbf{b})$ and the original region Ω . Motivated by the practical requirements in real-world applications, we distill two complementary error metrics. i) *Feasibility error*, denoted by e_{feas} , quantifies the extent to which the polytope \mathcal{P} exceeds the original region Ω ($e_{\text{feas}} = 0$ if and only if $\mathcal{P} \subseteq \Omega$, meaning that every point in \mathcal{P} is feasible with respect to Ω). ii) *Optimality error*, denoted by e_{opt} , measures the extent to which the original region Ω is not covered by the polytope \mathcal{P} ($e_{\text{opt}} = 0$ if and only if $\Omega \subseteq \mathcal{P}$, ensuring that any optimal solution attainable within Ω is also contained in \mathcal{P}). Both feasibility and optimality errors require computationally tractable formulations. To this end, we specify their directional counterparts, which quantify the feasibility and optimality errors along a given direction. Then, the feasibility and optimality errors are defined as the expectation of their directional counterparts over all directions (see ‘‘Error metrics’’ section in the Methods).

PolyFormer identifies a polytope $\mathcal{P}(\mathbf{A}, \mathbf{b})$ that best fits Ω by minimizing a weighted sum of the feasibility and optimality errors, as formulated by (2).

$$(\mathbf{A}^*, \mathbf{b}^*) = \underset{\mathbf{A} \in \mathbb{R}^{M \times n}, \mathbf{b} \in \mathbb{R}^M}{\arg \min} \lambda e_{\text{feas}} + (1 - \lambda) e_{\text{opt}}, \quad (2)$$

where $\lambda \in [0, 1]$ serves as a weight coefficient that controls the trade-off between the feasibility and optimality errors. By adjusting λ , we can control whether the learned polytope yields an inner approximation (a subset contained within the original region Ω , $\lambda = 1$), an outer approximation (a superset enclosing Ω , $\lambda = 0$), or an intermediate trade-off between the two ($0 < \lambda < 1$). This allows for flexibility in balancing the feasibility and optimality errors according to the specific application context. We will demonstrate this flexibility in the following three subsections by adjusting the weight coefficients for different problems.

PolyFormer can be trained efficiently because we derive an explicit loss function, differentiable with respect to \mathbf{A} and \mathbf{b} , based on the feasibility and optimality errors (see ‘‘Loss function and gradients’’ section in the Methods). The tailored loss function and its associated gradients reflect the core principle of PIML: they constitute physically informed formulations derived from geometric analyses of the discrepancy between the original region Ω and its polytopic approximation \mathcal{P} , which is particularly effective for the polytopic fitting task. This highlights a fundamental distinction between PolyFormer and most existing PIML approaches, in which physical loss functions are typically constructed from the residuals of governing equations [28–34]. By transforming an originally non-smooth geometric discrepancy into an explicitly differentiable objective, our formulation enables efficient gradient computation via standard automatic differentiation frameworks, such as PyTorch [38] or TensorFlow [39]. This further enables the use of gradient-based optimizers, such as stochastic gradient

descent (SGD) [40] and Adam [41], to update \mathbf{A} and \mathbf{b} . These methods outline the solution process for (2), i.e., the training procedure of PolyFormer, as illustrated in Fig. 1b. During training, when $\lambda \in (0, 1)$, the interaction between the feasibility and optimality objectives induces a dynamic balance that guides the polytope $\mathcal{P}(\mathbf{A}, \mathbf{b})$ toward a best-fit approximation of Ω .

The training procedure described above enables PolyFormer to fit a fixed target region Ω . However, many practical scenarios require repeatedly estimating regions that change with varying parameters, motivating the extension of PolyFormer to handle parameterized regions $\Omega(\boldsymbol{\theta})$ (where $\boldsymbol{\theta}$ denotes the varying parameters). Such parameters arise naturally in real-world applications. For instance, environmental factors such as temperature, humidity, and pressure in control systems, or socio-economic factors such as financial investments and population density in public service systems. To accommodate these scenarios, PolyFormer treats \mathbf{A} and \mathbf{b} as functions of $\boldsymbol{\theta}$, i.e., $\mathbf{A}(\boldsymbol{\theta})$ and $\mathbf{b}(\boldsymbol{\theta})$, which are fitted using neural networks, a well-established paradigm for solving high-dimensional fitting problems [40]. Training this neural network simply adds an sampling step over $\boldsymbol{\theta}$ to the aforementioned procedure, as illustrated in Fig. 1c. By incorporating varying parameters, PolyFormer attains greater adaptivity, enabling rapid re-estimation of the region following parameter updates and thereby substantially reducing computational costs in large-scale applications.

During PolyFormer training, the initialization, normalization, and selection of the weight coefficient λ can influence model performance. We outline our experimental strategies for these aspects in “Implementation remarks” section in the Methods to facilitate smooth deployment of PolyFormer in practice. To further clarify PolyFormer’s training process, its adaptation to changes in $\boldsymbol{\theta}$, and its scalability across dimensions, we evaluate PolyFormer on five representative geometries, including 2D polygons, ellipses, and non-convex regions, as well as 2 to 200-dimensional hypercubes and hyperspheres (see “Typical geometries” section in the Methods). We also provide a user guide in [Supplementary Note 1](#), which includes a detailed description of the PolyFormer workflow together with a step-by-step example to help readers quickly get started. Taken together, these practical guidelines, illustrative geometries, and hands-on instructions form a coherent toolkit that links the methodological design of PolyFormer with its effective use in practice, positioning PolyFormer as a ready-to-use framework for simplifying complex physical constraints and supporting scalable optimization in scientific discovery and engineering applications.

2.2 Aggregation of large-scale resources

The first challenge of solving real-world optimization problems that PolyFormer addresses is the complexity of numerous per-individual constraints, where each entity is governed by its own physical model and operational constraints. In such cases, aggregation techniques, i.e., representing a large number of entities using aggregated variables and constraints, are commonly employed to reduce model complexity [42]. Typical examples include logistics and delivery scheduling, where multiple orders are aggregated to enable efficient task assignment [3]; cloud computing resource management, where geographically proximate computing units are aggregated to support coordinated allocation [43]; and large-scale control systems, where the control capabilities

of individual devices are aggregated to define the boundaries for higher-level control signals [44–46]. Mathematically, aggregation corresponds to computing the Minkowski sum of multiple sets, which is generally NP-hard [47]. PolyFormer offers a tractable solution for approximating the aggregation, substantially reducing the complexity of handling large-scale, heterogeneous resources while preserving acceptable accuracy.

We consider the aggregation of feasible operational regions for controllable devices, including electric vehicles (EVs), battery storage systems (BSSs), and heat pumps (HPs). This is a highly active topic in smart grid applications for maintaining dynamic electricity supply-demand balance amid the proliferation of intermittent renewable energy throughout the modern energy system [45, 46]. In this context, to avoid infeasible dispatch caused by overestimation, an inner approximation (i.e., one with negligible feasibility error) of the true aggregated feasible region is desired. We examine two experimental scenarios: the first aggregates 1,000 resources with continuous control inputs; the second aggregates 105 resources with mixed continuous-discrete controls. The formal problem definition and descriptions of device models are provided in the “Apply PolyFormer to resource aggregation” section in the Methods, with detailed formulations and numerical settings in [Supplementary Note 3](#). Figs. 2a and 2b illustrate the evolution of feasibility and optimality errors during training in the two scenarios, respectively. In both scenarios, the PolyFormer model essentially converges to an inner approximation of the aggregated feasible region (demonstrated by the negligible feasibility errors: 7.1×10^{-15} for scenario (a) and 1.1×10^{-5} for scenario (b)).

To assess the quality of the inner approximation produced by PolyFormer, we benchmark it against the full model of all resources and two state-of-the-art aggregation techniques, namely the Box [45] and Homothet [46] methods. Fig. 2c reports the number of constraints (reflecting model complexity) and the optimality errors (reflecting conservatism) of different methods under the 1,000-resources case. Feasibility errors for all methods are below 10^{-5} and are therefore omitted. Although the full model is theoretically exact (with zero feasibility and optimality errors), it requires an extremely large number of constraints (57,696 constraints). The Homothet method fails to converge due to memory overflow, yielding no valid solution. The Box method has the minimum model complexity (only 48 constraints), but its optimality error is the highest, indicating a poor fit to the true aggregated region. In contrast, PolyFormer exhibits a small optimality error (approximately 21% of that of the Box method) while maintaining a small number of constraints (96 constraints, only 0.17% of the full model). This makes PolyFormer a compact yet accurate representation of the complex original region of all devices in the high-dimensional space.

In the second scenario, which involves discrete controls, the Box and Homothet methods are inherently inapplicable due to their structural limitations. To the best of our knowledge, PolyFormer is the only tractable approach capable of aggregating feasible regions under mixed continuous-discrete control. Note that although some resources are discretely controlled, resulting in integer components of the auxiliary variable \mathbf{y} in (1), the aggregated region Ω is still assumed to be continuous. This assumption is justified because the Minkowski sum with sufficiently rich continuous sets can bridge the gaps between disconnected sets, thereby finally yielding a continuous aggregated region [48]. Under this setting, PolyFormer maintains a small feasibility

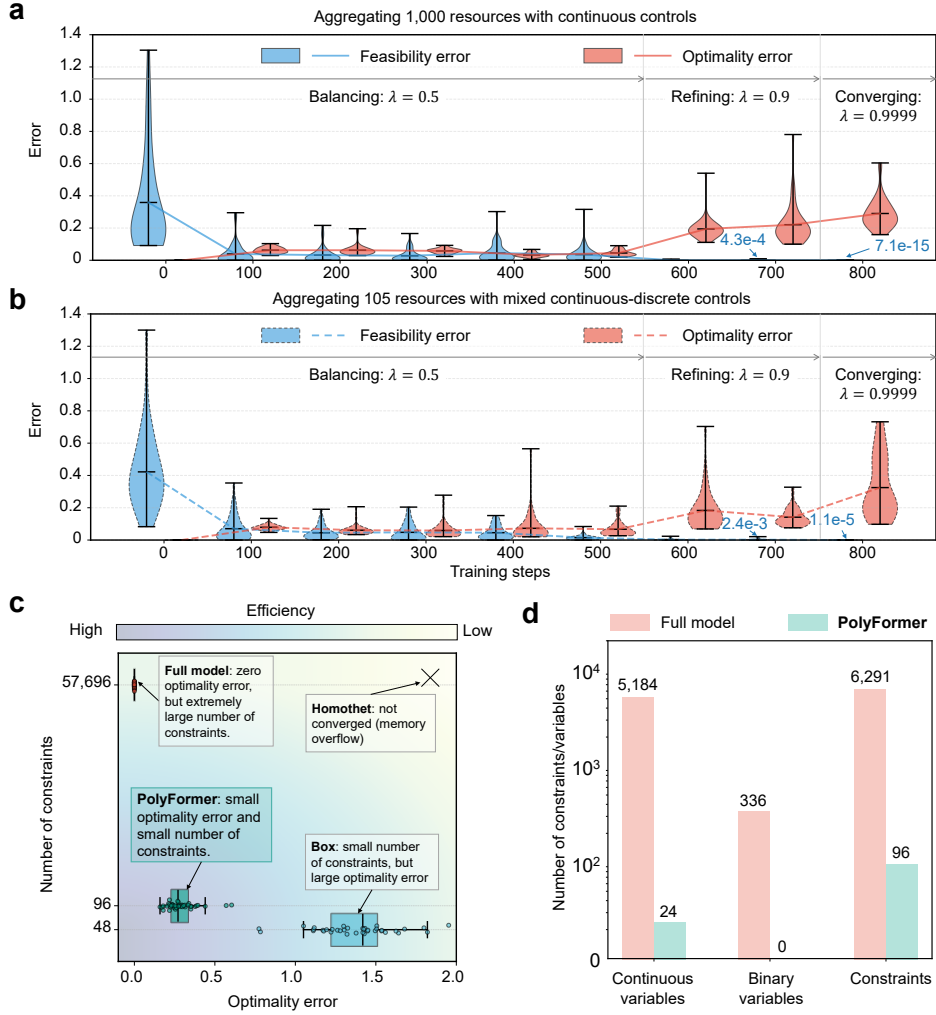


Fig. 2 Training process and benchmark results for large-scale resource aggregation. **a-b**, Evolution of the feasibility and optimality error distributions during PolyFormer training for two scenarios: (a) 1,000 resources with continuous controls and (b) 105 resources with mixed continuous-discrete controls. The error distributions are obtained by randomly sampling 50 directions and computing the directional errors according to (3) and (4). Training proceeds in three phases. In the balancing phase (iterations 1-500, $\lambda = 0.5$), both errors decrease as they compete with each other, and the polytope adapts to the true aggregated region. The refining phase (iterations 501-700, $\lambda = 0.9$) prioritizes feasibility while considering optimality to a lesser extent, reducing the average feasibility error to 4.3×10^{-4} and 2.4×10^{-3} , respectively. The converging phase (iterations 701-800, $\lambda = 0.9999$) drives feasibility errors to numerical zero (average 7.1×10^{-15} and 1.1×10^{-5} , respectively), enforcing an inner approximation. The total training time is 124 min (a) and 65 min (b). **c**, Modeling efficiency comparison among the full model, Box, Homothet, and PolyFormer in scenario (a), plotting optimality error (conservatism) versus number of constraints (complexity). The box plots show the distribution of optimality errors. Background shading from purple to yellow indicates decreasing efficiency in balancing complexity and conservatism, with the lower-left region most desirable. PolyFormer attains the best trade-off between complexity and conservatism. **d**, Complexity reduction from Full model to PolyFormer in scenario (b): PolyFormer removes all 336 binary variables and reduces continuous variables from 5,184 to 24 and constraints from 6,291 to 96.

error (1.1×10^{-5}) and achieves optimality errors comparable to those in the fully continuous scenario, indicating that the resulting aggregation is both reliable and not overly conservative. As shown in Fig. 2d, PolyFormer also significantly reduces model complexity relative to the full formulation: all binary variables are eliminated, the number of continuous variables is reduced by 99.54%, and the number of constraints decreases by 98.47%, demonstrating a substantial simplification of the original model.

In summary, PolyFormer enables a substantial reduction in model size when aggregating large populations of heterogeneous resources, while maintaining a tight inner approximation of the feasible region. This addresses the first challenge of scalable optimization, i.e., the large number of entities involved. In applications that require efficient management and control of large-scale resources, such as logistics networks [3], cloud computing infrastructures [43], large-scale control systems [44], and smart grids [45, 46], the efficient aggregation capability provided by PolyFormer offers broad practical potential.

2.3 Network-constrained optimization

We next apply PolyFormer to address the second type of complex physical constraints illustrated in Fig. 1a, i.e., network constraints that capture the interdependency among many entities. Optimization under large-scale network constraints is a common challenge in sectors like communications [4], energy [5], and transportation [6] systems, which are computationally expensive. Large-scale networks can often be decomposed into smaller subnetworks. For each subnetwork, PolyFormer learns a simplified polytopic constraint defined only over its boundary nodes. This polytopic set serves as a surrogate for the original subnetwork constraints. By replacing all subnetworks with their compact boundary representations, the overall problem size is significantly reduced, leading to substantial computational savings.

We consider the optimal power flow [14, 49, 50], a fundamental problem in electric power system operation, on a two-layer network comprising an upper-level transmission network and multiple lower-level distribution networks (Fig. 3a). The decision variables include the generation power in the transmission network, as well as the flexible power of nodes in the distribution networks. The optimization objective is to minimize the system’s total operating cost. Both levels are governed by nonlinear power flow equations due to the physical laws of electricity, and engineering requirements for network safety (see [Supplementary Note 4](#) for detailed formulations). An efficient solution to this problem has attracted increasing attention as the growing penetration of distributed renewable energy and the rapid expansion of large-scale computing facilities have significantly increased the interdependence and operational complexity of modern power systems [51]. Using PolyFormer, the thousands of nonlinear network constraints within each distribution network are compressed into only tens of linear constraints defined over the active and reactive power at the transmission-distribution interface (topologically, the root node; physically, the substation [52]). The full distribution-network model is then replaced by this compact boundary representation, so that the overall optimization problem scales only with the size of the transmission network. This reduction in constraint dimensionality leads to significant

improvement in computational efficiency (see “Apply PolyFormer to the two-layer power system optimization” section in the Methods).

The transmission and distribution network data are primarily obtained from the IEEE standard database [53], supplemented by the data from a real-world distribution system in Zhejiang Province, China. These datasets were combined to form a total of 27 cases of integrated transmission and distribution systems, see [Supplementary Note 4](#) for details. We compared the results with those obtained from solving the original full transmission-distribution optimization problem using IPOPT, a widely used open-source solver for large-scale nonlinear optimization [54]. Fig. 3b compares the solver time and peak memory usage for the PolyFormer-simplified network and full network optimization by IPOPT. PolyFormer delivers orders-of-magnitude improvements in computational efficiency across all test cases. For the largest system, the solver time is over $6,400\times$ faster, and memory usage decreases by 99.6%. This is achieved by simplifying the original model with 715,055 constraints and 477,691 variables into an approximate model containing only 2,239 constraints and 1,785 variables.

Fig. 3c reports the maximum feasibility error and the objective error under two different weight parameter settings. The feasibility error is defined as the largest deviation between the operating point (active and reactive power) at the root node obtained from the PolyFormer-simplified model and the nearest operating point that satisfies the original network constraints across all distribution networks. The objective error measures the relative difference in objective values between the PolyFormer-simplified optimization and the full network optimization. When the weight coefficient λ is set to 0.625, the average feasibility error is 2.6×10^{-6} , with a maximum below 10^{-4} . Increasing λ to 0.99 further improves feasibility: all feasibility errors fall below 10^{-8} , with an average of 6.4×10^{-10} (approximately four-order-of-magnitude reduction compared with the $\lambda = 0.625$ setting). This gain in feasibility is achieved at the cost of higher suboptimality. The average objective error increases from 3.7×10^{-5} to 7.2×10^{-4} , representing roughly a one-order-of-magnitude increase. Overall, these results quantify a clear feasibility-optimality trade-off controlled by λ : a four-order-of-magnitude reduction in constraint violations is obtained by accepting only a one-order-of-magnitude increase in objective error. Such a trade-off is attractive in applications where feasibility is prioritized over strict optimality [55].

These results highlight the exceptional performance of PolyFormer in solving large-scale nonlinear network-constrained optimization problems, demonstrating its ability to find solutions with strong feasibility and good optimality at a remarkably low computational cost. Such capabilities could bring benefits to various fields, including energy, communications, transportation systems, and others [4-6].

2.4 Optimization under uncertainty

Finally, we leverage PolyFormer to address the third type of complex constraints shown in Fig. 1a, namely uncertainty-related constraints. Accounting for uncertainty is important for optimization problems in many applications such as finance [56], transportation [57], control [58], supply chain management [59], machine learning [60], and others. Optimization under uncertainty aims to find robust policies that hedge against adversarial uncertainty realizations while allowing the decision-maker to tune the level

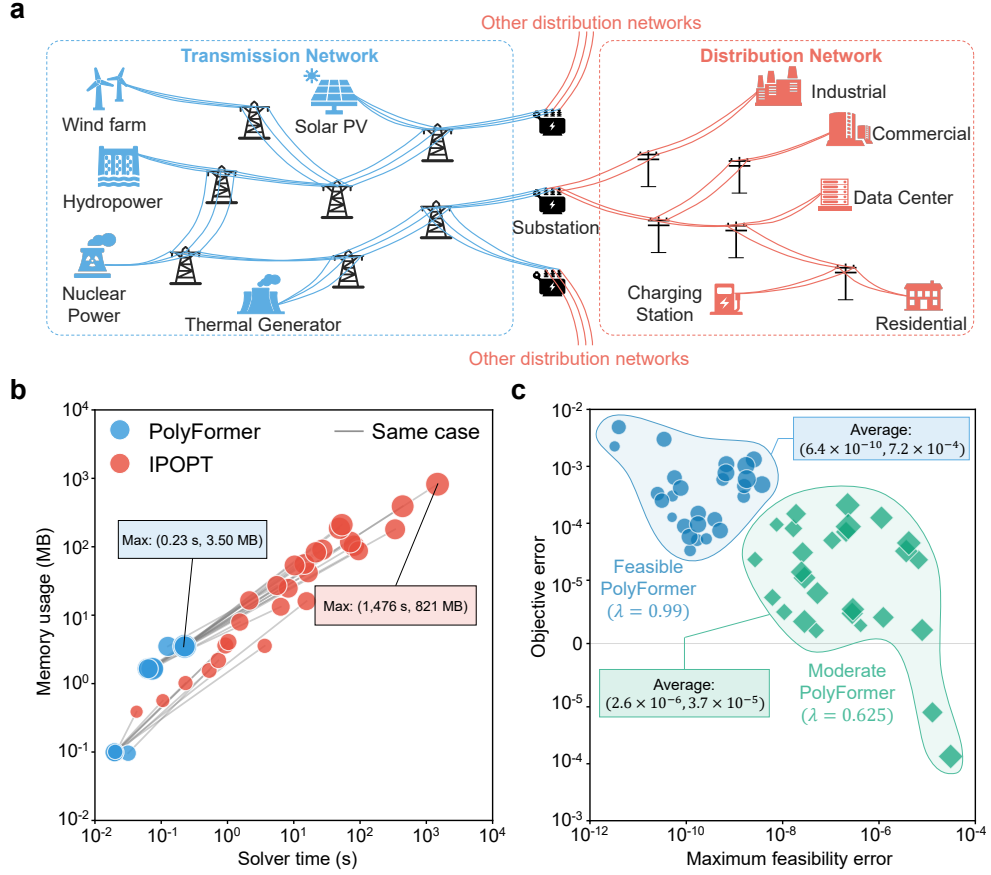


Fig. 3 Benchmark results of the two-layer power system optimization problem. **a**, Schematic diagram of the two-layer power system. The upper level transmission network includes generation units powered by various energy sources, transmitting electricity to substations. Then the distribution network distributes electricity to various users. **b**, Comparison of solver time and peak memory usage between optimization using the simplified PolyFormer model and optimization of the original full model solved by IPOPT. Each data point represents a transmission-distribution system case, with the size of the point indicating the case’s complexity (the total number of transmission and distribution nodes). Each red-blue pair represents the same case, with the connection from the upper-right red points to the lower-left blue points illustrating that PolyFormer consistently reduces both computation time and memory usage compared to directly solving the full problem with IPOPT. The largest case is also annotated in the figure: solving the original model takes 1,476 seconds and 821 MB of memory, while the PolyFormer-simplified model only requires 0.23 seconds and 3.50 MB of memory. **c**, Maximum feasibility error and objective error of two PolyFormer variants. All error values are normalized by dividing by the sum of squares of the baseline active and reactive powers of each distribution system. “Moderate PolyFormer” ($\lambda = 0.625$) yields an average maximum feasibility error of 2.6×10^{-6} and an average objective error of 3.7×10^{-5} . Two points show negative objective errors, indicating that the PolyFormer-simplified model yields lower costs than the original model. These points also have larger feasibility errors. “Feasible PolyFormer” ($\lambda = 0.99$) has all of the maximum feasibility errors below 10^{-8} , with an average of 6.4×10^{-10} . However, the average objective error is 7.2×10^{-4} , larger than that of Moderate PolyFormer, suggesting that the Feasible PolyFormer approach is more conservative, as expected.

of conservatism (i.e., the trade-off between nominal performance and risk protection). A recently popular framework is data-driven distributionally robust chance constraints (DRCCs), which infer an uncertainty distribution from finite samples and make decisions feasible with high probability even when the inferred distribution is misspecified [56–62]. Despite the practical appeal of DRCCs, they encounter considerable computational burdens [63, 64]. Although many DRCCs admit reformulations into linear (or conic-representable) constraints, these reformulations commonly depend on a large collection of auxiliary variables and constraints [61, 62], leading to substantial computational cost in large-scale problems. By contrast, PolyFormer yields a compact reformulation: it replaces the original DRCC with a small set of constraints expressed solely in terms of the original decision variables, thereby substantially reducing model complexity and improving computational efficiency.

In the previous two sections, we have focused on constraints arising from real physical systems, where prior knowledge is encoded through physics-based models. We now consider a portfolio optimization problem in finance to illustrate that the applicability of PolyFormer is not restricted to engineering or physical domains. Rather, its effectiveness stems from the geometric relationship between the original region and the approximate polytope, which does not necessarily originate from physical laws. Portfolio optimization is a fundamental topic in finance and is widely applied in the management of large-scale assets [65]. It seeks a portfolio allocation that maximizes the expected total return, subject to a prescribed risk tolerance, under the uncertain return of each asset [56, 66, 67]. Although financial markets are governed by socio-economic mechanisms rather than physical laws, the uncertainty-related risk constraints underlying them still induce a geometric region, which enables the application of PolyFormer to generate an effective simplification.

In our formulation, assets are partitioned into groups according to their risk levels. For each group, we impose a minimum return requirement under uncertainty, modeled as a distributionally robust chance constraint (DRCC): the probability that the group’s aggregate return falls below a prescribed threshold must not exceed a given risk level for all distributions in an ambiguity set constructed from data. Because multiple asset groups are considered, the overall portfolio problem contains multiple DRCCs coupled through the total investment constraint, leading to a computationally challenging formulation. PolyFormer is applied to approximate each group-level DRCC with a tractable surrogate, which is then embedded into the portfolio optimization problem (see “Apply PolyFormer to DRCC portfolio optimization” section in the Methods).

As a benchmark, we adopt the well-known Wasserstein-metric-based linear reformulation of DRCCs [62], hereafter referred to as “DRCC-linear.” The results obtained from the PolyFormer’s compact representation of DRCCs are compared with those obtained from the DRCC-linear model across four scenarios with different dimensionality, as shown in Fig. 4. In terms of model complexity, PolyFormer dramatically reduces the problem size from up to 1,044,497 constraints and 1,034,656 variables to 1,617 constraints and 400 variables, corresponding to reductions of over 99.8% and 99.9%, respectively. This contraction translates into significant computational savings: it reduces solution time from 513 s to 0.725 s (708× faster) and memory consumption from 938 MB to 1.20 MB (99.87% reduction). In terms of solution quality, PolyFormer

achieves non-inferior performance compared with DRCC-linear on average. Across all four scenarios shown in Fig. 4a-d, it attains smaller mean constraint violations, with higher returns in one case and only marginally lower returns in the remaining three. A comparison of the Pareto frontiers produced by the two methods shows that, in its best configurations, PolyFormer can generate solutions that dominate those of DRCC-linear, indicating simultaneous improvements in expected return and constraint violation. A possible explanation for this improvement lies in the different ways the two methods handle uncertainty samples. The PolyFormer-based reformulation removes the explicit dependence on the original uncertainty samples, and instead implicitly learns and embeds distributional information into the polytope’s geometry. In contrast, DRCC-linear builds constraints from the empirical sample distribution, reducing adaptability to distributional shifts in the test dataset, thereby degrading solution quality.

Overall, for optimization under uncertainty, PolyFormer compresses the large set of auxiliary variables and constraints into a small set of constraints defined only over the original decision variables. This yields a substantial simplification of uncertainty-related constraints while preserving solution quality, as evidenced by strong out-of-sample risk-return performance. In practical deployments, the decision-maker can change risk-control parameters (e.g., confidence levels, conservatism factors) to generate multiple candidate portfolio strategies and select the most desirable trade-off between risk and return. With state-of-the-art methods such as DRCC-linear, each strategy computation can be prohibitively expensive. By contrast, PolyFormer enables rapid instantiation across parameter values and hence efficient generation and evaluation of many strategies. This capability markedly reduces the computational burden of large-scale optimization under uncertainty. Although PolyFormer is here evaluated on the portfolio optimization problem in a financial context, optimization under uncertainty is pervasive across fields like transportation [57], control [58], robotics [20], supply chain management [59], and machine learning [60]. Given its effectiveness in handling uncertainty-related constraints, PolyFormer has the potential to substantially advance decision-making in real-world settings where data are limited, noisy, or partially observed.

3 Discussion

This work introduces PolyFormer, which reveals a new capability of PIML in prescriptive tasks: it can substantially simplify complex constraints in large-scale optimization problems, thereby significantly reducing computational burden. PolyFormer combines the expressive power of machine learning with the reliability and solver-compatibility of classical optimization methods. In doing so, it provides a unified framework to address three fundamental challenges in large-scale optimization: aggregating numerous per-individual constraints into compact representations, projecting complex network dependencies onto manageable boundaries, and reformulating uncertainty-related constraints without introducing excessive auxiliary variables or constraints.

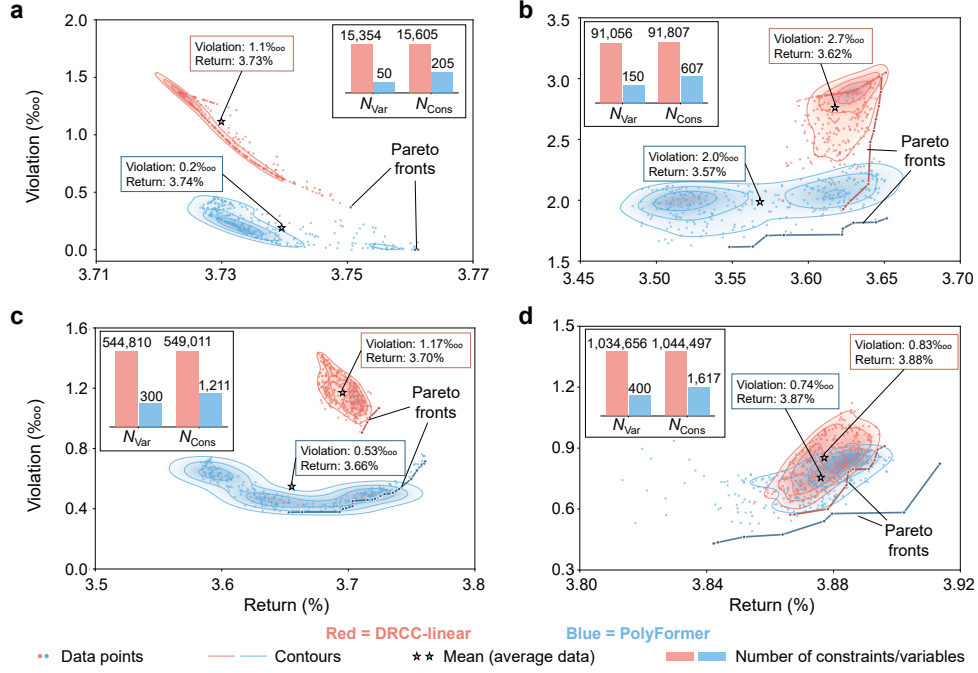


Fig. 4 Benchmark results of DRCC portfolio optimization across four case settings. **a**, 50 assets, 2 groups, 150 samples. **b**, 150 assets, 3 groups, 300 samples. **c**, 300 assets, 5 groups, 900 samples. **d**, 400 assets, 8 groups, 1280 samples. Each scatter plot shows the return rate versus average constraint violation for 300 portfolio strategies solved using the DRCC-linear and PolyFormer models. Data points represent the average constraint violation and actual return of a portfolio strategy evaluated on a test dataset of 100 uncertain return samples (see [Supplementary Note 4](#)). The strategies are derived from varying parameters (risk level, Wasserstein ball radius, maximum group investment cap, and minimum acceptable return per group), as described in the “Apply PolyFormer to DRCC portfolio optimization” section in the Methods. Contours, averages, and Pareto fronts are annotated in the plots. Solutions with higher returns and lower errors (i.e., located towards the bottom-right) are considered better. Notably, in all four cases, PolyFormer consistently finds a large number of non-inferior solutions compared to DRCC-linear in the bottom-left area, while also identifying superior solutions in the bottom-right area, indicating the high quality of the solutions produced by PolyFormer. The bar charts in each subfigure compare the number of variables and constraints for the two methods in each case. PolyFormer significantly reduces the number of variables (by 99.67% to 99.99%) and constraints (by 98.69% to 99.85%) compared to DRCC-linear in all cases, leading to a substantial decrease in computational complexity.

Extensive additional experiments were conducted across a range of problem settings, including diverse resource aggregation scenarios, two-layer power system optimization under varying operating conditions, and large-scale portfolio optimization with different asset and grouping settings. Across these tasks, PolyFormer demonstrates consistently strong and stable performance. These results suggest that PolyFormer captures general principles of constraint simplification with a robust performance across domains, scales, and parameter settings.

Looking forward, PolyFormer aligns with broader efforts to integrate domain knowledge and machine learning for solving various constrained optimization problems. The framework is inherently extensible, with clear pathways for incorporating richer prior information, more expressive learning architectures, and tighter integration with modern optimization pipelines. Methodological extensions, including adaptive sampling methods for nonconvex regions and enhanced uncertainty handling, may further strengthen its robustness, particularly in safety-critical applications.

The full implementation of PolyFormer is publicly available (see ‘‘Code Availability’’), enabling reproducibility and further development. As constrained optimization problems continue to grow in complexity and importance across scientific, engineering, and socio-economic systems, we anticipate PolyFormer-based solutions to play an increasingly central role in bridging the gap between realistic modeling and scalable computation.

4 Methods

4.1 Error metrics

Since \mathcal{P} and Ω are two bounded geometric bodies in \mathbb{R}^n , their discrepancy can be classically characterized by the Hausdorff distance [68]. However, the Hausdorff distance is non-smooth and, in general, entails NP-hard computational complexity, which makes it unsuitable for optimizing the parameters \mathbf{A} and \mathbf{b} . This limitation motivates the introduction of alternative error metrics with improved smoothness and computational efficiency, rendering them more favorable to gradient-based training. The computational burden of the Hausdorff distance primarily stems from the maximization over pointwise discrepancies between the two sets. Nevertheless, such a worst-case characterization is not essential for identifying a well-fitting polytope. In practice, discrepancies distributed across different directions of the polytope and the original region provide informative signals for updating the polytope parameters, rather than relying solely on the point attaining the maximum deviation.

In light of this observation, we introduce *directional error*, which quantifies the extent to which \mathcal{P} and Ω exceed one another along a given direction $\mathbf{v} \in \mathbb{R}^n \setminus \mathbf{0}$, defined as follows:

$$e_{\text{feas}}(\mathbf{v}) = \min_{\mathbf{z} \in \Omega} \|\mathbf{z} - \mathbf{x}'\|^2, \text{ s.t., } \mathbf{x}' = \arg \max_{\mathbf{x} \in \mathcal{P}(\mathbf{A}, \mathbf{b})} \mathbf{v}^\top \mathbf{x}, \quad (3)$$

$$e_{\text{opt}}(\mathbf{v}) = \min_{\mathbf{x} \in \mathcal{P}(\mathbf{A}, \mathbf{b})} \|\mathbf{x} - \mathbf{z}'\|^2, \text{ s.t., } \mathbf{z}' = \arg \max_{\mathbf{z} \in \Omega} \mathbf{v}^\top \mathbf{z}, \quad (4)$$

where, $e_{\text{feas}}(\mathbf{v})$ denotes the directional feasibility error, defined as the sum of squared distances by which \mathcal{P} exceeds Ω in the direction \mathbf{v} , while $e_{\text{opt}}(\mathbf{v})$ represents the directional optimality error, corresponding to the sum of squared distances by which Ω exceeds \mathcal{P} in the direction \mathbf{v} .

In (3) and (4), the lower-level subproblems compute the support points of \mathcal{P} and Ω along the direction \mathbf{v} , respectively. Consequently, if Ω is nonconvex, the optimality error defined in (4) cannot capture concave regions of Ω . This explains why PolyFormer

may ultimately converge to an approximation of the convex hull of Ω . Nevertheless, in (3), the upper-level projection can reach a point \mathbf{z} located in the concave boundaries of Ω , so the overall effect is not restricted to convex-hull approximations.

Both $e_{\text{feas}}(\mathbf{v})$ and $e_{\text{opt}}(\mathbf{v})$ can be computed by solving two independent single-level subproblems and therefore do not introduce additional computational complexity beyond the original region Ω . In particular, as long as linear and quadratic objectives can be solved efficiently over the original region Ω (using open-source or commercial solvers such as Gurobi [69], IPOPT [54], and BARON [70]), the evaluation of the directional errors can be carried out efficiently.

Then, the feasibility and optimality errors are specified as the expectations of their directional counterparts over directions \mathbf{v} drawn from the standard n -dimensional Gaussian distribution, i.e.,

$$e_{\text{feas}} = \mathbb{E}_{\mathbf{v} \sim \mathcal{N}(0, I_n)} e_{\text{feas}}(\mathbf{v}), \quad e_{\text{opt}} = \mathbb{E}_{\mathbf{v} \sim \mathcal{N}(0, I_n)} e_{\text{opt}}(\mathbf{v}). \quad (5)$$

Sampling $\mathbf{v} \sim \mathcal{N}(0, I_n)$ ensures that all directions in \mathbb{R}^n are uniformly explored. This expectation-based formulation directly motivates the training strategy. At each iteration, a random direction \mathbf{v} is sampled and the corresponding directional errors $e_{\text{feas}}(\mathbf{v})$ and $e_{\text{opt}}(\mathbf{v})$ are evaluated. The polytope \mathcal{P} is then updated to reduce the discrepancy with Ω along the sampled direction. By repeatedly sampling directions and refining \mathcal{P} , the weighted error $\lambda e_{\text{feas}} + (1 - \lambda) e_{\text{opt}}$ is minimized in expectation. Although each directional evaluation requires solving four optimization problems, the entire training phase is performed offline and thus allows sufficient computational time. Once trained, the resulting polytope \mathcal{P} can be directly embedded into optimization problems, leading to substantial gains in computational efficiency during online deployment.

4.2 Loss function and gradients

This section derives an explicit loss function for training \mathbf{A} and \mathbf{b} based on the directional error calculations. Taking the directional feasibility error in (3) as an example, suppose the lower-level linear program attains its optimum at \mathbf{x}' , and let \mathbf{z}^* denote the optimal solution of the upper-level projection problem. The directional feasibility error $e_{\text{feas}}(\mathbf{v})$ is determined by \mathbf{x}' and \mathbf{z}^* , both of which depend implicitly on \mathbf{A} and \mathbf{b} . Therefore, computing the gradient of $e_{\text{feas}}(\mathbf{v})$ with respect to \mathbf{A} and \mathbf{b} requires applying implicit differentiation, which leads to nontrivial derivative expressions. Although such gradients can be obtained automatically using tools such as CVXPYLayers [71], this approach requires that all $g_j(\mathbf{x}, \mathbf{y})$, $j = 1, 2, \dots, m$, be convex and that both \mathbf{x} and \mathbf{y} are continuous variables, limiting its generality. Moreover, computing implicit differentiation involves large matrix inversions, which increase computational cost and may affect numerical stability.

Given that the primary role of the loss function is to identify which hyperplanes of the polytope \mathcal{P} should be updated and to provide information about the update directions, it is then not necessary to exactly compute the gradient of the directional error formulations with respect to \mathbf{A} and \mathbf{b} . Therefore, for better generality, Polyformer does not directly use the directional error formulations as the loss function, but instead adopts an explicitly differentiable approximation. To identify the hyperplanes to be

updated, we note that only those hyperplanes active at the point \mathbf{x}' determine its local variation. We therefore restrict updates to the hyperplanes of \mathcal{P} that are active at \mathbf{x}' , indexed by the set J . The system $\mathbf{A}_J \mathbf{x} = \mathbf{b}_J$ defines a hyperplane arrangement whose intersection yields \mathbf{x}' . For the update direction, a natural strategy is to move the hyperplane arrangement $\mathbf{A}_J \mathbf{x} = \mathbf{b}_J$ toward the point \mathbf{z}^* in the original region Ω , thereby shifting their intersection \mathbf{x}' closer to \mathbf{z}^* . We therefore quantify the squared distance from \mathbf{z}^* to the hyperplane arrangement $\mathbf{A}_J \mathbf{x} = \mathbf{b}_J$ and adopt it as the feasibility-error loss. Assuming that each row of \mathbf{A} is unit-normalized, this loss is defined as

$$L_{\text{feas}}(\mathbf{A}, \mathbf{b}; \mathbf{v}) = \|\mathbf{A}_J \mathbf{z}^* - \mathbf{b}_J\|^2. \quad (6)$$

In fact, we have $L_{\text{feas}}(\mathbf{A}, \mathbf{b}; \mathbf{v}) = e_{\text{feas}}(\mathbf{v}) \sum_{j \in J} \cos^2 \phi_j$ by geometric analysis, where $\phi_j (\forall j \in J)$ is the angle between the vector $\mathbf{z}^* - \mathbf{x}'$ and the normal vector \mathbf{A}_j . This indicates that $L_{\text{feas}}(\mathbf{A}, \mathbf{b}; \mathbf{v})$ and $e_{\text{feas}}(\mathbf{v})$ are positively correlated, and minimizing $L_{\text{feas}}(\mathbf{A}, \mathbf{b}; \mathbf{v})$ can also reduce $e_{\text{feas}}(\mathbf{v})$.

In (6), \mathbf{z}^* is a boundary point of the original region Ω that is close to the hyperplane arrangement $\mathbf{A}_J \mathbf{x} = \mathbf{b}_J$. Although variations in \mathbf{A}_J and \mathbf{b}_J may indeed shift \mathbf{z}^* to a different boundary point, updating the hyperplane arrangement $\mathbf{A}_J \mathbf{x} = \mathbf{b}_J$ in the direction of the current \mathbf{z}^* still moves the boundary of \mathcal{P} closer to the boundary of Ω . For computational efficiency, we therefore ignore the implicit dependence of \mathbf{z}^* on \mathbf{A} and \mathbf{b} , and treat \mathbf{z}^* as a fixed point. Under this approximation, the gradients of $L_{\text{feas}}(\mathbf{A}, \mathbf{b}; \mathbf{v})$ with respect to \mathbf{A} and \mathbf{b} can be computed as follows:

$$\nabla_{\mathbf{A}_j} L_{\text{feas}}(\mathbf{A}, \mathbf{b}; \mathbf{v}) = \begin{cases} 2(\mathbf{A}_j^\top \mathbf{z}^* - b_j) \mathbf{z}^{*\top}, & j \in J \\ \mathbf{0}^\top, & \text{otherwise} \end{cases}, \quad (7)$$

$$\nabla_{b_j} L_{\text{feas}}(\mathbf{A}, \mathbf{b}; \mathbf{v}) = \begin{cases} -2(\mathbf{A}_j^\top \mathbf{z}^* - b_j), & j \in J \\ 0, & \text{otherwise} \end{cases}. \quad (8)$$

Similar derivations can be made for the optimality error $e_{\text{opt}}(\mathbf{v})$. Assume that the upper-level projection problem of (4) attains an optimum at \mathbf{x}^* , whose active constraints are indexed by K , i.e., $\mathbf{A}_K \mathbf{x}^* = \mathbf{b}_K$. Let \mathbf{z}' denote the optimal solution of the lower-level problem, then the optimality-error loss is defined as:

$$L_{\text{opt}}(\mathbf{A}, \mathbf{b}; \mathbf{v}) = \|\mathbf{A}_K \mathbf{z}' - \mathbf{b}_K\|^2. \quad (9)$$

with gradients given by:

$$\nabla_{\mathbf{A}_k} L_{\text{opt}}(\mathbf{A}, \mathbf{b}; \mathbf{v}) = \begin{cases} 2(\mathbf{A}_k^\top \mathbf{z}' - b_k) \mathbf{z}'^\top, & k \in K \\ \mathbf{0}^\top, & \text{otherwise} \end{cases}, \quad (10)$$

$$\nabla_{b_k} L_{\text{opt}}(\mathbf{A}, \mathbf{b}; \mathbf{v}) = \begin{cases} -2(\mathbf{A}_k^\top \mathbf{z}' - b_k), & k \in K \\ 0, & \text{otherwise} \end{cases}. \quad (11)$$

By assigning the weight coefficient λ to the two losses, we can construct the overall loss function for PolyFormer as:

$$\begin{aligned} L_{\text{total}}(\mathbf{A}, \mathbf{b}; \mathbf{v}) &= \lambda L_{\text{feas}}(\mathbf{A}, \mathbf{b}; \mathbf{v}) + (1 - \lambda) L_{\text{opt}}(\mathbf{A}, \mathbf{b}; \mathbf{v}) \\ &= \lambda \|\mathbf{A}_J \mathbf{z}^* - \mathbf{b}_J\|^2 + (1 - \lambda) \|\mathbf{A}_K \mathbf{z}' - \mathbf{b}_K\|^2. \end{aligned} \quad (12)$$

and the corresponding gradients are:

$$\nabla_{\mathbf{A}} L_{\text{total}}(\mathbf{A}, \mathbf{b}; \mathbf{v}) = \lambda \nabla_{\mathbf{A}} L_{\text{feas}}(\mathbf{A}, \mathbf{b}; \mathbf{v}) + (1 - \lambda) \nabla_{\mathbf{A}} L_{\text{opt}}(\mathbf{A}, \mathbf{b}; \mathbf{v}), \quad (13)$$

$$\nabla_{\mathbf{b}} L_{\text{total}}(\mathbf{A}, \mathbf{b}; \mathbf{v}) = \lambda \nabla_{\mathbf{b}} L_{\text{feas}}(\mathbf{A}, \mathbf{b}; \mathbf{v}) + (1 - \lambda) \nabla_{\mathbf{b}} L_{\text{opt}}(\mathbf{A}, \mathbf{b}; \mathbf{v}). \quad (14)$$

We have thus obtained an explicitly differentiable loss function with respect to \mathbf{A} and \mathbf{b} . In practice, it is unnecessary to manually compute the gradients according to (13) and (14). Instead, we only need to define the loss function as in (12) and call automatic differentiation tools, such as PyTorch or TensorFlow, to obtain the gradients. Standard gradient-based optimization algorithms, e.g., SGD or Adam, can then be employed to train the PolyFormer model. Notably, for different directions \mathbf{v} , computing directional errors via (3) and (4) may activate different index sets J and K . As the training iteration proceeds, each hyperplane of \mathcal{P} has the opportunity to be updated, ultimately enabling \mathcal{P} to approximate the original region Ω as closely as possible across all directions.

The loss function (12) and gradients (13) and (14) can be straightforwardly extended to the case of parameterized regions, i.e., $\Omega(\boldsymbol{\theta})$. Specifically, we replace \mathbf{A} and \mathbf{b} with differentiable mappings $\mathbf{A}(\boldsymbol{\theta})$ and $\mathbf{b}(\boldsymbol{\theta})$, respectively. The gradients with respect to $\boldsymbol{\theta}$ can then be computed automatically using the chain rule. In our implementation of PolyFormer, two neural networks, i.e., \mathbf{A} -net and \mathbf{b} -net, are employed to parameterize $\mathbf{A}(\boldsymbol{\theta})$ and $\mathbf{b}(\boldsymbol{\theta})$, respectively, and all training procedures are carried out using PyTorch [38].

4.3 Implementation remarks

Here, we provide three important remarks to facilitate a smooth implementation of PolyFormer.

Remark 1 (Initialization) The initial approximate polytope must be nonempty. We can first initialize \mathbf{A} either randomly or based on the physical characteristics of the problem, and then initialize \mathbf{b} by solving $b_j = \max_{\mathbf{x} \in \Omega} \mathbf{A}_j \mathbf{x}$, $1 \leq j \leq M$. This approach outputs an outer approximation ($e_{\text{opt}} = 0$) as the initial polytope. In the presence of parameters $\boldsymbol{\theta}$, the initialization only requires setting $\boldsymbol{\theta}$ to the mean of its distribution or dataset to compute the corresponding values for \mathbf{A} and \mathbf{b} . Then, in the neural networks that fit $\mathbf{A}(\boldsymbol{\theta})$ and $\mathbf{b}(\boldsymbol{\theta})$, all coefficients are initialized to zero, except for the bias terms, which are initialized with the initial values of \mathbf{A} and \mathbf{b} .

Remark 2 (Normalization) As mentioned in the derivation of the loss function and gradients (6)-(14), the row vectors of \mathbf{A} need to be normalized throughout the entire training process. This can be achieved by dividing each row vector of \mathbf{A} and the corresponding element of \mathbf{b}

by the norm of that row vector after each update of \mathbf{A} and \mathbf{b} . We also recommend normalizing each dimension of the original variable \mathbf{x} and the parameter $\boldsymbol{\theta}$ (if there are any), e.g., constraining each dimension of \mathbf{x} and $\boldsymbol{\theta}$ within $[0, 1]$, which can improve the training stability and convergence speed.

Remark 3 (Setting λ) The weight coefficient λ controls the emphasis on feasibility and optimality during training. Typically, we recommend starting with a balanced value, e.g., $\lambda = 0.5$, so that the feasibility error and optimality error can compete with each other to identify the shape that best matches the original region Ω . After training for enough iterations, λ can be adjusted based on the specific requirements of the practical scenario. For example, in most optimization scenarios where high feasibility is desired, λ should be increased to ensure a small enough feasibility error.

4.4 Typical geometries

To help better understand the training procedure of PolyFormer and how its outputs adapt to the varying parameters, we provide three illustrative examples, i.e., polygons, ellipses, and nonconvex regions, that offer an intuitive introduction to PolyFormer. In addition, to demonstrate PolyFormer’s accuracy and scalability, we also implemented PolyFormer on two benchmark cases with known global optima (hypercubes and hyperspheres). The numerical settings for all cases in this section are provided in [Supplementary Note 2](#).

In the three 2D cases, we use PolyFormer to obtain a quadrilateral approximation of an octagon, a hexagonal approximation of an ellipse, and a hexagonal approximation of a nonconvex region (a portion of a disk that does not intersect another disk). As shown in [Extended Data Fig. 1a](#), the approximating polygons evolve over successive iterations, exhibiting a trade-off between feasibility and optimality errors, and converge to shapes that closely match the original regions in all three cases. When introducing varying parameters $\boldsymbol{\theta}$, the underlying feasible set becomes parameter-dependent. [Extended Data Fig. 1b-d](#) shows that the true feasible region deforms smoothly as $\boldsymbol{\theta}$ varies, and, correspondingly, the parameterized PolyFormer produces polytopes that adapt coherently to these changes. Notably, in the nonconvex case, the final polygon fits the convex hull of the original nonconvex region, which has been stated in the “Error metrics” section in the Methods. While this highlights a limitation of the current PolyFormer, convex hulls are adequate in many applications [72–74]. In applications where tighter feasibility guarantees are required for nonconvex sets, extending the sampling strategy to capture a convex inner approximation, e.g., via fixed-point rays, offers a natural direction for future work.

In the hypercube case, the target feasible set is an n -dimensional hypercube, and the approximate polytope is constructed with $M = 2n$ hyperplanes. In our experimental cases, the approximation converges to the exact hypercube with arbitrarily small error given sufficient training, consistent with the fact that the global optimal approximation error is zero. [Extended Data Fig. 2a](#) reports the initial error across dimensions and the number of training steps needed for the total error to drop below 10^{-5} . Increasing dimensionality leads to larger initial errors and slower convergence, with both quantities exhibiting approximately polynomial scaling in n .

In the hypersphere case, the target feasible set is an n -dimensional unit sphere, and the approximate polytope again uses $M = 2n$ hyperplanes. This setting admits a global optimal total error of $1 - \frac{2\sqrt{n}}{n+1}$ (given $\lambda = 0.5$). [Extended Data Fig. 2b](#) summarizes the initial error, converged error, ideal error, and the error-reduction rate attained by PolyFormer. Although PolyFormer does not attain the exact global optimum, it achieves an error reduction exceeding 99.4% across all tested dimensions. Notably, in higher-dimensional regimes ($n \geq 30$), the error reduction consistently surpasses 99.9%.

4.5 Apply PolyFormer to resource aggregation

We study the aggregation of feasible power regions for EVs, HPs, and BSSs, a task that arises commonly in smart grid applications [45, 46]. Let \mathcal{I}_{EV} , \mathcal{I}_{BSS} and \mathcal{I}_{HP} denote the corresponding resource sets, indexed by i . Let $\mathbf{p}_i = [p_{i,1}, \dots, p_{i,T}]^\top \in \mathbb{R}^T$ denote the power trajectory of resource i (with load treated as positive), where $T = 24$ represents a 24-hour horizon.

Each resource is subject to specific physical and technology constraints that define an individual feasible region Ω_i for its power trajectory: $\mathbf{p}_i \in \Omega_i, \forall i \in \mathcal{I}_{\text{EV}} \cup \mathcal{I}_{\text{BSS}} \cup \mathcal{I}_{\text{HP}}$. The exact definitions of Ω_i for each resource type are provided in [Supplementary Note 3](#). We aim to characterize the feasible region of the aggregated power trajectory $\mathbf{P} = [P_1, \dots, P_T]^\top \in \mathbb{R}^T$, defined by the Minkowski sum [47, 48]:

$$\Omega = \left\{ \mathbf{P} \in \mathbb{R}^T \left| \begin{array}{l} P_t = \sum_{i \in \mathcal{I}_{\text{EV}} \cup \mathcal{I}_{\text{BSS}} \cup \mathcal{I}_{\text{HP}}} p_{i,t}, \quad \forall t \in \{1, 2, \dots, T\} \\ \mathbf{p}_i \in \Omega_i, \quad \forall i \in \mathcal{I}_{\text{EV}} \cup \mathcal{I}_{\text{BSS}} \cup \mathcal{I}_{\text{HP}} \end{array} \right. \right\}. \quad (15)$$

The aggregated power trajectory \mathbf{P} corresponds to the decision variable \mathbf{x} in Equation (1) with dimension $n = T$, and the collection of individual trajectories $\mathbf{p}_i, \forall i \in \mathcal{I}_{\text{EV}} \cup \mathcal{I}_{\text{BSS}} \cup \mathcal{I}_{\text{HP}}$ corresponds to the auxiliary variable \mathbf{y} with dimension $n' = T(|\mathcal{I}_{\text{EV}}| + |\mathcal{I}_{\text{BSS}}| + |\mathcal{I}_{\text{HP}}|)$.

We apply PolyFormer to construct a polytopic inner approximation of Ω , using $M = 4T$ hyperplanes (rows of \mathbf{A}). This case does not involve varying parameters, so we directly optimize \mathbf{A} and \mathbf{b} following the training pipeline in Fig. 1b. The training proceeds in three phases (see the caption of Fig. 2), and finally outputs an inner approximation that guarantees the feasibility of disaggregation of any aggregated trajectory into implementable resource-level schedules. Detailed numerical settings are provided in [Supplementary Note 3](#).

4.6 Apply PolyFormer to the two-layer power system optimization

In the two-layer power system optimization problem, both levels are governed by nonlinear power-flow constraints. Specifically, the upper-level transmission network is modeled via the standard AC power-flow equations [75], while the lower-level distribution network adopts the DistFlow formulation [76] (see [Supplementary Note 4](#) for details). Within each distribution network, a subset of nodes can flexibly adjust active

and reactive power injections within prescribed bounds through demand-response programs or controllable resources (e.g., distributed generation and energy storage) [77]. The combination of these flexibility envelopes and the network operating constraints induces a feasible set for the active-reactive power exchange at the transmission-distribution (T-D) interface. In practice, distribution networks are typically operated in a radial topology [78], with the T-D interface corresponding to the root node of the distribution network (physically, a substation). Electrical consistency requires that the active power, reactive power, and voltage magnitude (per unit) at the transmission-side interconnection node coincide with the corresponding variables at the distribution root node. Variations in the root-node voltage propagate along the feeder and may push downstream nodal voltages beyond their allowable limits, thereby reshaping the admissible active-reactive power region at the root node. Consequently, the root-node feasible region in the (P, Q) plane is inherently voltage-dependent. We denote this parametric feasible set by $(P, Q) \in \Omega(V)$, where P , Q , and V represent the root-bus active power, reactive power, and voltage magnitude, respectively.

We employ PolyFormer to approximate the voltage-parameterized feasible region $\Omega(V)$ of each distribution network by a polytope described through linear inequalities that depend only on the root-node power injections (P, Q) . Accordingly, PolyFormer operates in a two-dimensional decision space ($n = 2$). We fix the number of hyperplanes by setting the row dimension of \mathbf{A} to $M = 8$. In this setting, the sole varying parameter is the voltage magnitude V ; hence, the neural networks used to parameterize $\mathbf{A}(\theta)$ and $\mathbf{b}(\theta)$ take a one-dimensional input.¹ The network architecture consists of a single fully connected hidden layer with 128 neurons and ReLU activation placed between the input and output layers. During training, we uniformly sample V over its admissible interval, i.e., $[0.95, 1.05]$ p.u., to generate a diverse set of operating conditions. The detailed numerical configuration is provided in [Supplementary Note 4](#). After training, the learned polytopical approximations are embedded directly into the transmission-level optimization, replacing the original distribution network constraints $\Omega(V)$.

4.7 Apply PolyFormer to DRCC portfolio optimization

The DRCC portfolio optimization is formulated as follows:

$$\max \quad \sum_{i=1}^N \tilde{r}_i x_i \quad (16a)$$

$$\text{s.t.} \quad \inf_{\mathbb{P} \in \mathcal{Q}} \mathbb{P} \left(\sum_{i \in \mathcal{N}_g} \tilde{r}_i x_i \geq R_g \sum_{i \in \mathcal{N}_g} x_i \right) \geq 1 - \epsilon_g, \quad g = 1, 2, \dots, G, \quad (16b)$$

$$\sum_{i=1}^N x_i \leq 1, \quad (16c)$$

$$\sum_{i \in \mathcal{N}_g} x_i \leq X_g^{\max}, \quad \forall i \in \mathcal{N}_g, \quad g = 1, 2, \dots, G, \quad (16d)$$

¹In practical distribution networks, the feasible power region of the root node may also be influenced by the power fluctuations at each node. In such cases, the power of all or certain key nodes can be chosen as varying parameters to expand the input dimensions of the neural network. However, this does not affect the validation of PolyFormer's performance in network-constrained optimization, so the simplified version using only the root node voltage as input is employed here.

where the decision variable $x_i \in \mathbb{R}_+$ represents the proportion of investment in asset i ; the uncertain variable \tilde{r}_i denotes the random return of asset i , and \bar{r}_i denotes its expectation; N is the total number of assets; G is the total number of asset groups; \mathcal{N}_g is the set of assets in group g ; R_g is the minimum acceptable return for group g ; ϵ_g is the risk level for group g ; X_g^{\max} is the maximum allowable investment proportion for group g ; and \mathcal{Q} represents the ambiguity set of probability distributions for the uncertain returns, defined using the Wasserstein distance with radius ρ_g centered at the empirical distribution derived from a historical dataset of size K [61].

The objective function (16a) maximizes the expected return of the portfolio. The DRCC (16b) ensures that, for each asset group, the probability of the portfolio return falling below the specified minimum acceptable return does not exceed the given risk level ϵ_g , considering the worst-case distribution within the ambiguity set. Constraint (16c) limits the total investment and constraint (16d) enforces the group-wise investment caps. The challenge of solving this problem lies in the complexity of the DRCCs (16b), which involve infinite-dimensional optimization over probability distributions. We first apply an analytical reformulation to convert the DRCCs into a finite set of linear constraints [62], as detailed in [Supplementary Note 5](#). Then, we use PolyFormer to approximate these reformulated constraints with a small number of linear inequalities involving only the decision variables x_i .

The variable dimension for the PolyFormer used to approximate the DRCC of asset group g is $n = |\mathcal{N}_g|$, and the number of rows of the matrix \mathbf{A} is set to $M = 4n + 2$. There are four parameters for each asset group: the risk level ϵ_g , the ambiguity-set radius ρ , the minimum acceptable return R_g , and the groupwise investment cap X_g^{\max} . Therefore, the input dimension for the neural networks that parameterize $\mathbf{A}(\boldsymbol{\theta})$ and $\mathbf{b}(\boldsymbol{\theta})$ is 4. We add a fully connected hidden layer with 128 neurons and ReLU activation between the input and output. During training, we randomly sample these four varying parameters within predefined ranges to generate diverse training scenarios. The specific parameter ranges and other numerical settings are detailed in [Supplementary Note 5](#). When the training is complete, the learned polytopes are directly embedded into the portfolio optimization problem to replace the original DRCCs (16b).

Acknowledgements. This work is funded by the National Natural Science Foundation of China under Grant Numbers 52507091 and U24B2080; Smart Grid-National Science and Technology Major Project under Grant Number 2024ZD0801700; China Postdoctoral Science Foundation under Grant Number GZC20250335; State Key Laboratory of Power System Operation and Control under Grant Number SKLD25KZ04. We thank G. Hug for valuable discussions and guidance in the design of experiments.

Author contributions. Y.W. conceived the idea. Y.W. and Y.G. developed the theory and methods. Y.W. implemented the algorithms. B.Z. acquired the data and provided the experimental conditions. Y.W., Y.G., and W.Q. conducted the numerical studies and analysis. Y.W., Y.G., and W.Q. prepared the figures. All authors contributed to data analysis, discussions, and manuscript preparation.

Competing interests. The authors declare no competing interests.

Code availability. All the data and code are made openly available at <https://github.com/wenyl16/PolyFormer>.

References

- [1] Chen, S.W., Wang, T., Atanasov, N., Kumar, V., Morari, M.: Large scale model predictive control with neural networks and primal active sets. *Automatica* **135**, 109947 (2022)
- [2] Zhou, X., Wen, X., Wang, Z., Gao, Y., Li, H., Wang, Q., Yang, T., Lu, H., Cao, Y., Xu, C., Gao, F.: Swarm of micro flying robots in the wild. *Science Robotics* **7**(66), 5954 (2022)
- [3] Liang, Y., Luo, H., Duan, H., Li, D., Liao, H., Feng, J., Zhao, J., Ren, H., Ding, X., Cha, Y., Zhou, Q., Situ, C., Hao, J., Xing, K., Yin, F., He, R., Sun, Y., Zheng, Y., Feng, Y., Sun, Z., Chen, J., Zheng, J., Wang, L.: Meituan’s real-time intelligent dispatching algorithms build the world’s largest minute-level delivery network. *INFORMS Journal on Applied Analytics* **54**(1), 84–101 (2024)
- [4] Wu, J., Tse, C.K., Lau, F.C.M.: Optimizing performance of communication networks: An application of network science. *IEEE Transactions on Circuits and Systems II: Express Briefs* **62**(1), 95–99 (2015)
- [5] Millinger, M., Hedenus, F., Zeyen, E., Neumann, F., Reichenberg, L., Berndes, G.: Diversity of biomass usage pathways to achieve emissions targets in the European energy system. *Nature Energy* **10**(2), 226–242 (2025)
- [6] Yim, K.K.W., Wong, S.C., Chen, A., Wong, C.K., Lam, W.H.K.: A reliability-based land use and transportation optimization model. *Transportation Research Part C: Emerging Technologies* **19**(2), 351–362 (2011)
- [7] Fischhoff, B., Davis, A.L.: Communicating scientific uncertainty. *Proceedings of the National Academy of Sciences* **111**(supplement 4), 13664–13671 (2014)
- [8] Chester, M.V., Underwood, B.S., Samaras, C.: Keeping infrastructure reliable under climate uncertainty. *Nature Climate Change* **10**(6), 488–490 (2020)
- [9] Shen, H., Jiang, R.: Convex chance-constrained programs with wasserstein ambiguity. *Operations Research* **73**(4), 2264–2280 (2025)
- [10] International Energy Agency: Global EV Outlook 2025, Paris (2025). <https://www.iea.org/reports/global-ev-outlook-2025>
- [11] Batlle, C., Barruso, M., Rodilla, P., Canoyra, A.: The (hopefully) enlightening blackout in spain: Questions and lessons for the future. MIT CEEPR Research Commentary (2025)
- [12] Adulyasak, Y., Cordeau, J.-F., Jans, R.: Benders decomposition for production routing under demand uncertainty. *Operations Research* **63**(4), 851–867 (2015)

- [13] Boyd, S., Parikh, N., Chu, E., Peleato, B., Eckstein, J.: Distributed optimization and statistical learning via the alternating direction method of multipliers. *Foundations and Trends® in Machine Learning* **3**(1), 1–122 (2011)
- [14] Dai, X., Zhai, J., Jiang, Y., Guo, Y., Jones, C.N., Hagenmeyer, V.: Advancing distributed AC optimal power flow for integrated transmission-distribution systems. *IEEE Transactions on Network Science and Engineering* **12**(2), 1210–1223 (2025)
- [15] Chandrasekaran, V., Jordan, M.I.: Computational and statistical tradeoffs via convex relaxation. *Proceedings of the National Academy of Sciences* **110**(13), 1181–1190 (2013)
- [16] Low, S.H.: Convex relaxation of optimal power flow—part i: Formulations and equivalence. *IEEE Transactions on Control of Network Systems* **1**(1), 15–27 (2014)
- [17] Bemporad, A., Filippi, C.: An algorithm for approximate multiparametric convex programming. *Computational Optimization and Applications* **35**(1), 87–108 (2006)
- [18] Jones, C.N., Morari, M.: Polytopic approximation of explicit model predictive controllers. *IEEE Transactions on Automatic Control* **55**(11), 2542–2553 (2010)
- [19] Wen, Y., Hu, Z., You, S., Duan, X.: Aggregate feasible region of DERs: Exact formulation and approximate models. *IEEE Transactions on Smart Grid* **13**(6) (2022)
- [20] Wu, P., Chen, J.: Data-driven polytopic approximation for an n -dimensional probabilistic reachable set. *IEEE Transactions on Industrial Informatics* **20**(9), 11192–11201 (2024)
- [21] Donti, P.L., Rolnick, D., Kolter, J.Z.: DC3: A learning method for optimization with hard constraints. In: *International Conference on Learning Representations (ICLR)* (2021)
- [22] Wei, Y., Peng, B., Xie, R., et al.: Deep active optimization for complex systems. *Nature Computational Science*, 1–12 (2025)
- [23] He, H., Daumé, H., Eisner, J.: Learning to search in branch and bound algorithms. In: *Advances in Neural Information Processing Systems*, vol. 27. Curran Associates, Inc., Montreal, Canada (2014)
- [24] Baker, K.: Learning warm-start points for ac optimal power flow. In: *2019 IEEE 29th International Workshop on Machine Learning for Signal Processing (MLSP)*, pp. 1–6 (2019). IEEE

- [25] Shen, Z.-S., Pan, F., Wang, Y., et al.: Free-energy machine for combinatorial optimization. *Nature Computational Science*, 1–11 (2025)
- [26] Wang, Y., Wang, J., Zhang, H., Song, J.: Bridging prediction and decision: Advances and challenges in data-driven optimization. *Nexus* **2**(1), 100057 (2025)
- [27] Karniadakis, G.E., Kevrekidis, I.G., Lu, L., Perdikaris, P., Wang, S., Yang, L.: Physics-informed machine learning. *Nature Reviews Physics* **3**(6), 422–440 (2021)
- [28] Raissi, M., Yazdani, A., Karniadakis, G.E.: Hidden fluid mechanics: Learning velocity and pressure fields from flow visualizations. *Science* **367**(6481), 1026–1030 (2020)
- [29] Rao, C., Ren, P., Wang, Q., Buyukozturk, O., Sun, H., Liu, Y.: Encoding physics to learn reaction-diffusion processes. *Nature Machine Intelligence* **5**(7), 765–779 (2023)
- [30] Feng, Z., Chen, J., Hai, Y., Pang, X., Zheng, K., Xie, C., Zhang, X., Li, S., Zhang, C., Liu, K., Zhu, L., Hu, X., Li, S., Zhang, J., Zhang, K., Li, H.: Sliding-attention transformer neural architecture for predicting T cell receptor–antigen–human leucocyte antigen binding. *Nature Machine Intelligence* **6**(10), 1216–1230 (2024)
- [31] Venturella, C., Li, J., Hillenbrand, C., Leyva Peralta, X., Liu, J., Zhu, T.: Unified deep learning framework for many-body quantum chemistry via Green’s functions. *Nature Computational Science* **5**(6), 502–513 (2025)
- [32] Singh, A., Gaurav, K.: Piml-sm: Physics-informed machine learning to estimate surface soil moisture from multisensor satellite images by leveraging swarm intelligence. *IEEE Transactions on Geoscience and Remote Sensing* **62**, 1–13 (2024)
- [33] Senhora, F.V., Chi, H., Zhang, Y., Mirabella, L., Tang, T.L.E., Paulino, G.H.: Machine learning for topology optimization: Physics-based learning through an independent training strategy. *Computer Methods in Applied Mechanics and Engineering* **398**, 115116 (2022)
- [34] Patel, R., Bhartiya, S., Gudi, R.: Model predictive control using physics informed neural networks for process systems. *IFAC-PapersOnLine* **58**(14), 775–780 (2024)
- [35] Bauschke, H.H., Borwein, J.M.: On projection algorithms for solving convex feasibility problems. *SIAM Review* **38**(3), 367–426 (1996)
- [36] AryaRahul, AryaSunil, D, d.F., MountDavid: Optimal bound on the combinatorial complexity of approximating polytopes. *ACM Transactions on Algorithms* (2022)
- [37] Rockafellar, R.T.: *Convex Analysis*. Princeton Mathematical Series, vol. 28.

Princeton University Press, Princeton, NJ (1970)

- [38] Paszke, A., Gross, S., Massa, F., *et al.*: Pytorch: An imperative style, high-performance deep learning library. In: *Advances in Neural Information Processing Systems*, vol. 32. Curran Associates, Inc., Vancouver, Canada (2019)
- [39] Abadi, M., Barham, P., Chen, J., Chen, Z., Davis, A., Dean, J., Devin, M., Ghemawat, S., Irving, G., Isard, M., *et al.*: Tensorflow: A system for large-scale machine learning. In: *12th {USENIX} Symposium on Operating Systems Design and Implementation ({OSDI} 16)*, pp. 265–283 (2016)
- [40] Rumelhart, D.E., Hinton, G.E., Williams, R.J.: Learning representations by back-propagating errors. *Nature* **323**(6088), 533–536 (1986)
- [41] Kingma, D.P., Ba, J.: Adam: A method for stochastic optimization. In: *3rd International Conference on Learning Representations, ICLR 2015, Conference Track Proceedings, San Diego, USA* (2015)
- [42] Rogers, D.F., Plante, R.D., Wong, R.T., Evans, J.R.: Aggregation and disaggregation techniques and methodology in optimization. *Operations Research* **39**(4), 553–582 (1991)
- [43] Khezri, E., Yahya, R.O., Hassanzadeh, H., Mohaidat, M., Ahmadi, S., Trik, M.: DLJSF: Data - locality aware job scheduling IoT tasks in fog-cloud computing environments. *Results in Engineering* **21**, 101780 (2024)
- [44] Fattahi, A.: Utilities’ managed home charging programs for electric vehicles. *Management Science (Articles in Advance)*, 1–20 (2025)
- [45] Chen, X., Dall’Anese, E., Zhao, C., Li, N.: Aggregate power flexibility in unbalanced distribution systems. *IEEE Transactions on Smart Grid* **11**(1), 258–269 (2020)
- [46] Wang, S., Wu, W.: Aggregate flexibility of virtual power plants with temporal coupling constraints. *IEEE Transactions on Smart Grid* **12**(6), 5043–5051 (2021)
- [47] Tiwary, H.R.: On the hardness of computing intersection, union and Minkowski sum of polytopes. *Discrete & Computational Geometry* **40**(3), 469–479 (2008)
- [48] Schneider, R.: *Convex Bodies: The Brunn-Minkowski Theory*. Cambridge University Press, Cambridge (2013)
- [49] Donon, B., Maziarz, A., Valko, M.: Learning optimal power flow with graph neural networks. *Nature Machine Intelligence* **6**, 66–75 (2024)
- [50] Burchett, R.C., Happ, H.H., Wirgau, K.A.: Large scale optimal power flow. *IEEE Transactions on Power Apparatus and Systems* **PAS-101**(10), 3722–3732 (1982)

- [51] Colangelo, P., Coskun, A.K., Megrue, J., Roberts, C., Sengupta, S., Sivaram, V., Tiao, E., Vijaykar, A., Williams, C., Wilson, D.C., Records, B., MacFarland, Z., Dreiling, D., Morey, N., Ratnayake, A., Vairamohan, B.: AI data centres as grid-interactive assets. *Nature Energy* (2025)
- [52] International Electrotechnical Vocabulary (IEV) – Part 605: Generation, Transmission and Distribution of Electricity – Substations. International Electrotechnical Commission. <https://webstore.iec.ch/en/publication/231> Accessed 2025-12-19
- [53] Zimmerman, R.D., Murillo-Sanchez, C.E.: MATPOWER (Version 8.1). <https://matpower.org>
- [54] Wächter, A., Biegler, L.T.: On the implementation of an interior-point filter line-search algorithm for large-scale nonlinear programming. *Mathematical Programming* **106**(1), 25–57 (2006)
- [55] Stern, R., Dreiman, G., Valenzano, R.: Probably bounded suboptimal heuristic search. *Artificial Intelligence* **267**, 39–57 (2019)
- [56] Chen, Z., Kuhn, D., Wiesemann, W.: Technical note—data-driven chance constrained programs over wasserstein balls. *Operations Research* **72**(1), 410–424 (2024)
- [57] Wang, C., Liu, K., Zhang, C., Miao, L.: Distributionally robust chance-constrained optimization for the integrated berth allocation and quay crane assignment problem. *Transportation Research Part B: Methodological* **182**, 102923 (2024)
- [58] Coulson, J., Lygeros, J., Dörfler, F.: Distributionally robust chance constrained data-enabled predictive control. *IEEE Transactions on Automatic Control* **67**(7), 3289–3304 (2022)
- [59] Gao, Y., Lu, S., Zhan, S., Hu, C., Liu, X.: Closed-loop supply chain network design with price-greenness-sensitive demand: A distributionally robust chance-constrained optimization approach. *Computers & Operations Research* **172**, 106803 (2024)
- [60] Lin, F., Fang, S.-C., Fang, X., Gao, Z.: Distributionally robust chance-constrained kernel-based support vector machine. *Computers & Operations Research* **170**, 106755 (2024)
- [61] Xie, W.: On distributionally robust chance constrained programs with Wasserstein distance. *Mathematical Programming* **186**(1), 115–155 (2021)
- [62] Ordoudis, C., Nguyen, V.A., Kuhn, D., Pinson, P.: Energy and reserve dispatch with distributionally robust joint chance constraints. *Operations Research Letters*

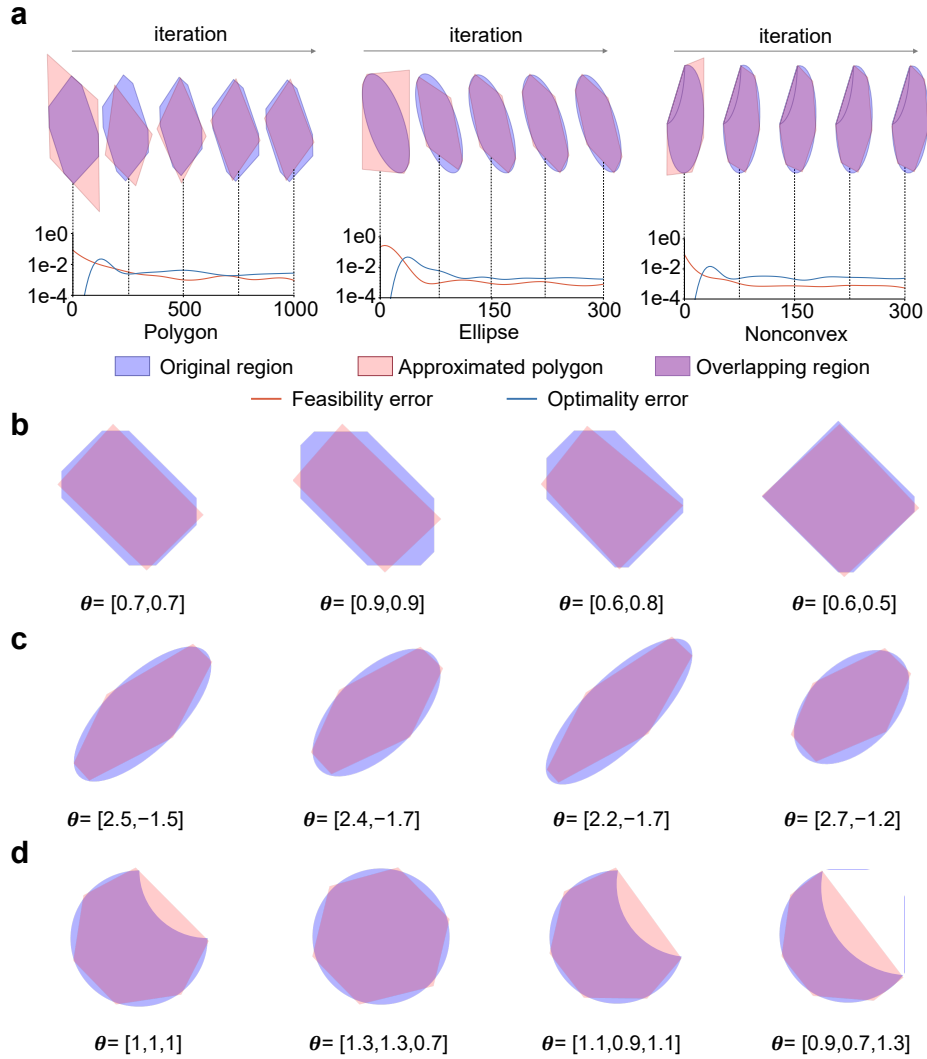
49(3), 291–299 (2021)

- [63] Shang, C., Wang, C., You, K., Huang, D.: Distributionally robust chance constraint with unimodality-skewness information and conic reformulation. *Operations Research Letters* **50**(2), 176–183 (2022)
- [64] Ho-Nguyen, N., Kılınç-Karzan, F., Küçükyavuz, S., Lee, D.: Distributionally robust chance-constrained programs with right-hand side uncertainty under Wasserstein ambiguity. *Mathematical Programming* **196**(1), 641–672 (2022)
- [65] Fabozzi, F.J., Gupta, F., Markowitz, H.M.: The legacy of modern portfolio theory. *The Journal of Investing* **11**(3), 7–22 (2002)
- [66] Mohajerin Esfahani, P., Kuhn, D.: Data-driven distributionally robust optimization using the Wasserstein metric: performance guarantees and tractable reformulations. *Mathematical Programming* **171**(1), 115–166 (2018)
- [67] Xie, W., Ahmed, S.: Bicriteria approximation of chance-constrained covering problems. *Operations Research* **68**(2), 516–533 (2020)
- [68] Jungeblut, P., Kleist, L., Miltzow, T.: The complexity of the hausdorff distance. *Discrete & Computational Geometry* **71**(1), 177–213 (2024)
- [69] Gurobi Optimization, LLC: Gurobi Optimizer Reference Manual. (2025)
- [70] Sahinidis, N.V.: BARON: A general purpose global optimization software package. *Journal of Global Optimization* **8**(2), 201–205 (1996)
- [71] Agrawal, A., Amos, B., Barratt, S., Boyd, S., Diamond, S., Kolter, Z.: Differentiable convex optimization layers. In: *Advances in Neural Information Processing Systems* (2019)
- [72] Yang, R., Liu, X.: Convex hull relaxation of optimal control problems with general nonconvex control constraints. *IEEE Transactions on Automatic Control* **69**(6), 4028–4034 (2024)
- [73] De Rosa, A., Khajavirad, A.: Explicit convex hull description of bivariate quadratic sets with indicator variables. *Mathematical Programming* (2024)
- [74] Adams, W.P., Sherali, H.D.: A hierarchy of relaxations leading to the convex hull representation for general discrete optimization problems. *Annals of Operations Research* **140**(1), 21–47 (2005)
- [75] Tinney, W.F., Hart, C.E.: Power flow solution by newton’s method. *IEEE Transactions on Power Apparatus and Systems* **PAS-86**(11), 1449–1460 (1967)
- [76] Baran, M.E., Wu, F.F.: Network reconfiguration in distribution systems for loss

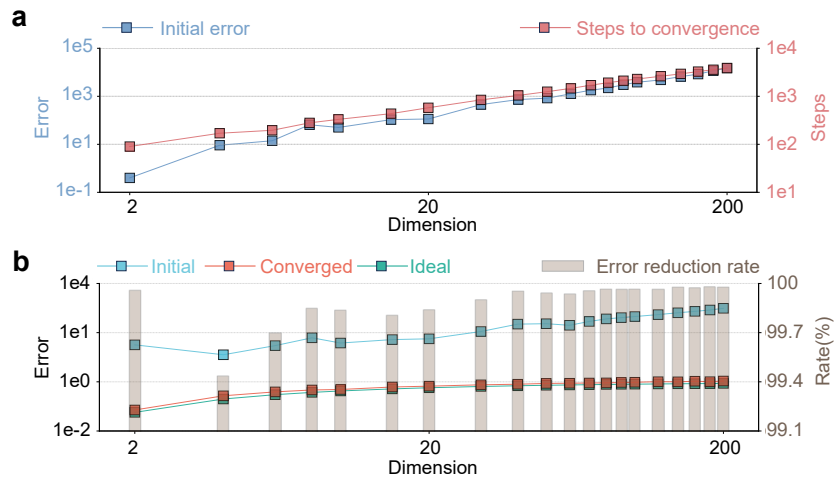
reduction and load balancing. *IEEE Transactions on Power Delivery* **4**(2), 1401–1407 (1989)

[77] Jackson, R., Zhou, E., Reyna, J.: Building and grid system benefits of demand flexibility and energy efficiency. *Joule* **5**(8), 1927–1930 (2021)

[78] Deka, D., Kekatos, V., Cavraro, G.: Learning distribution grid topologies: A tutorial. *IEEE Transactions on Smart Grid* **15**(1), 999–1013 (2024)



Extended Data Fig. 1 Illustrative results for three 2D cases. **a**, Evolution of training errors and corresponding geometric shapes for polygonal, elliptical, and nonconvex regions, evaluated with all varying parameters fixed at their baseline values. As feasibility and optimality errors compete during training, the approximated regions progressively converge toward the original region. **b-d**, PolyFormer fitting results under varying parameters for the polygon (b), ellipse (c), and nonconvex (d) cases. Changes in the parameters induce deformations of the original regions, which are consistently tracked by the approximating polygons.



Extended Data Fig. 2 Benchmark results for two multi-dimensional cases. a, Hypercube benchmark. For all tested dimensions, the final total error falls below 10^{-5} , indicating convergence. Both the initial total error (left) and the number of steps to convergence (right) increase with dimensionality, following an approximately polynomial scaling. **b**, Hypersphere benchmark. Although the global optimum is not attained, the method consistently converges to near-optimal solutions. Line plots show the initial, converged, and ideal total errors, while bar charts report the error reduction rate from initialization to convergence. Across all dimensions, the total error is reduced by more than 99.4%, exceeding 99.9% when $n \geq 30$.